

Nature Methods

Elastic Volume Reconstruction from Series of Ultra-thin Microscopy Sections

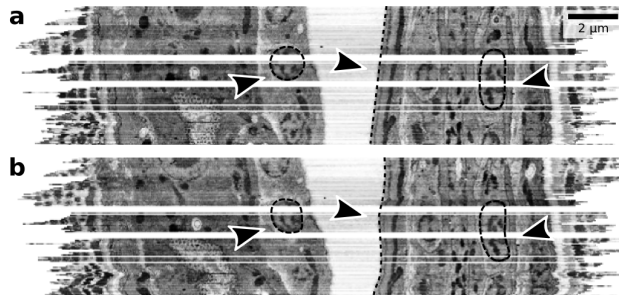
Stephan Saalfeld, Richard Fetter, Albert Cardona & Pavel Tomancak

Supplementary File	Title
Supplementary Figure 1	Comparison of elastic alignment exploring eight adjacent sections or only direct neighbors.
Supplementary Figure 2	Typical artifacts that inevitably occur in large TEM series.
Supplementary Figure 3	Local block matching filters.
Supplementary Figure 4	The number of filtered matches can be used to detect artifacts and missing sections.
Supplementary Figure 5	Spring forces.
Supplementary Figure 6	Elastic montaging compensates for nonrigid deformation.
Supplementary Figure 7	Comparison of average section scale factors after alignment of the evaluation series.
Supplementary Figure 8	Histograms of absolute point displacements after alignment of evaluation series A and B.
Supplementary Figure 9	Projection of the x,y location of each z point of a sample of straight lines projected through the volume along the z axis.
Supplementary Figure 10	Projection of the x,z location of each z point of a sample of straight lines projected through the volume along the z axis.
Supplementary Figure 11	Histograms of section-to-section pairwise point displacements after alignment of evaluation series A and B.
Supplementary Figure 12	Visualization of section-to-section pairwise point displacements after alignment of evaluation series A and B.
Supplementary Figure 13	Anatomical context of the <i>Drosophila</i> larval ventral nerve cord TEM section series.
Supplementary Figure 14	Synapses are detectable in both lateral and axial views after elastic reconstruction.
Supplementary Figure 15	Comparison of three alignment methods applied to the <i>Drosophila</i> series using the total length of manual skeleton annotation.
Supplementary Figure 16	Total skeleton length and lower bound skeleton length.
Supplementary Table 1	Overview of reconstructed ssTEM datasets.
Supplementary Note	Additional technical information on the elastic registration method, the description of serial section data sets presented in the manuscript and details on implementation and availability of the software.

Note: Supplementary Videos 1–14 are available on the Nature Methods website.

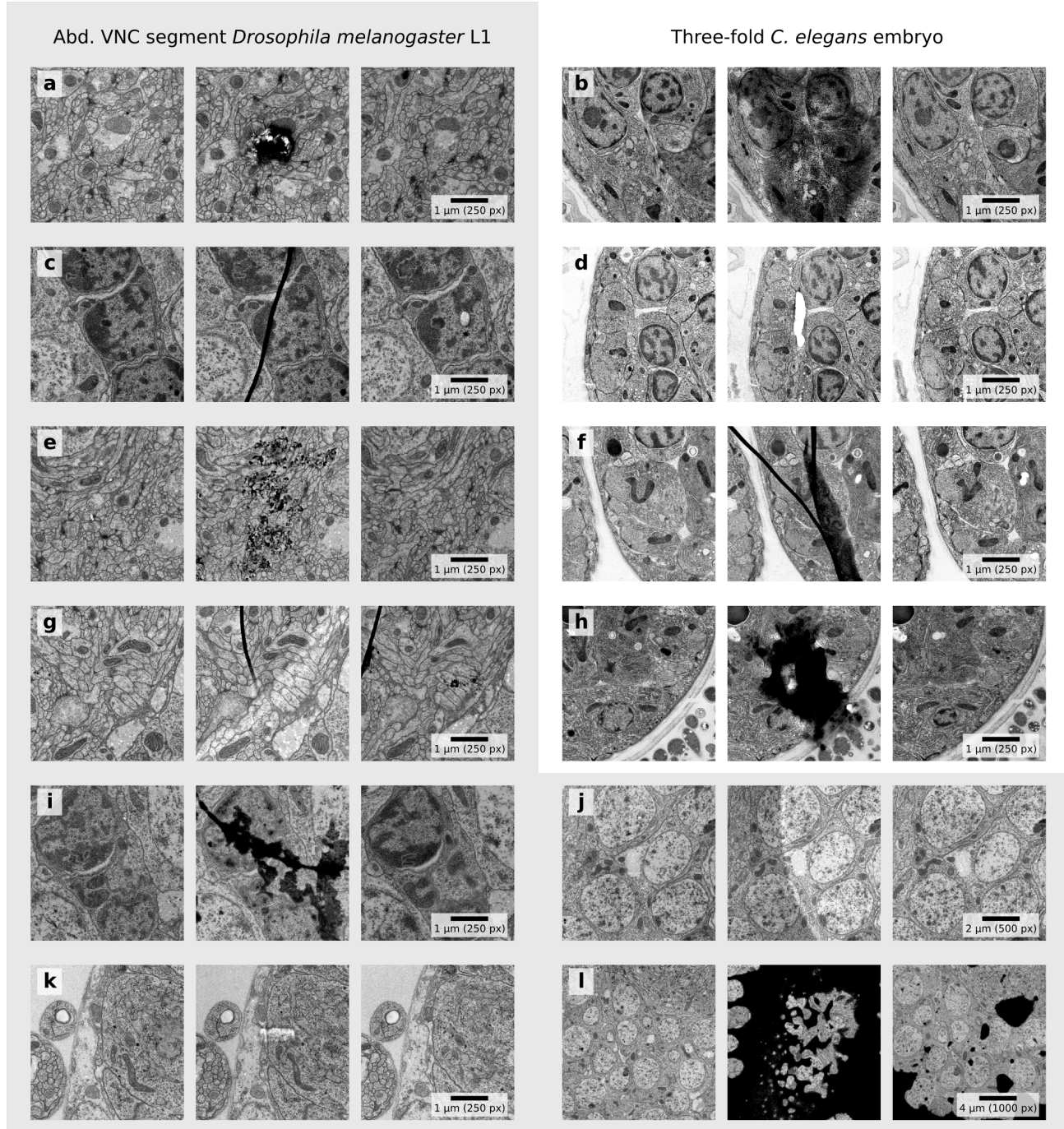
Supplementary Figures

Supplementary Figure 1 | Comparison of elastic alignment exploring eight adjacent sections or only direct neighbors.



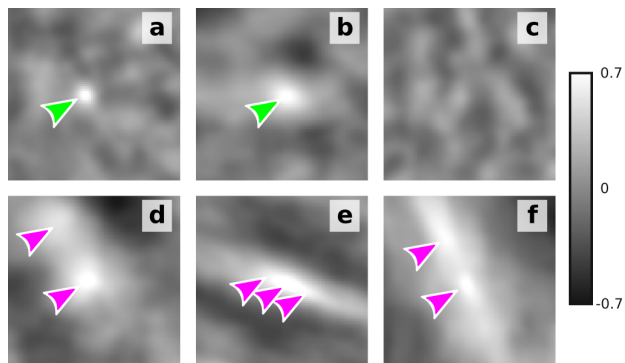
An axial virtual slice of a subset of sections through a three-fold stage *C. elegans* embryo (two parts of the same folded embryo are visible) that were aligned elastically connecting each section either to a local neighborhood of 8 sections (**a**) or only to its directly adjacent sections (**b**). Alignment using a larger local neighborhood (**a**) outperforms alignment where only direct neighbors were used (**b**); the nuclei adopt smooth oval shape even in the presence of missing sections (white bands across) and vertical features are continuous and straight (arrowheads). The apparently jagged edges on each side are the result of each section image covering a slightly different field of view at arbitrary orientation. In the aligned staple, images overlap only partially.

Supplementary Figure 2 | Typical artifacts that inevitably occur in large TEM series.



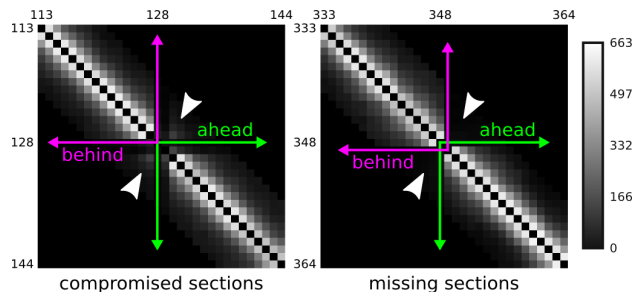
Snapshots of the elastically aligned *Drosophila* and *C. elegans* series show a section compromised by an artifact in context with adjacent sections. Some artifacts impact image similarity but have no effect on geometry (dirt (**a,h**), staining precipitates (**a,b,e,i,l**), support film folds (**f,g,i**), illumination variance (**g,j**)). Others distort local geometry (section folds (**c**), stretches (**g,k**), cracks (**d,k**))).

Supplementary Figure 3 | Local block matching filters.



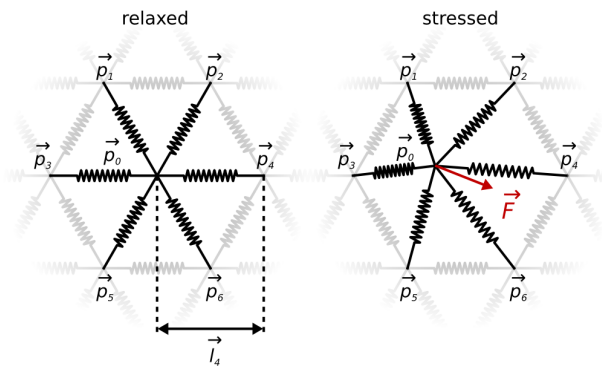
Shown is the NCC coefficient r of a block of image /1 over a reference image /2 for all translational offsets in a square region with the coordinate origin in the center. Coefficients r are displayed as gray values (see scale). The candidate for the sought after translational offset is the location with maximal r (**a,b**). Candidates are rejected if either r was below a given threshold (**c**; not similar), there was more than one maximum with very similar r (**d,f**; ambiguous), or the maximum is not well localized in both dimensions (**e,f**; an edge pattern that fits everywhere alongside the edge).

Supplementary Figure 4 | The number of filtered matches can be used to detect artifacts and missing sections.



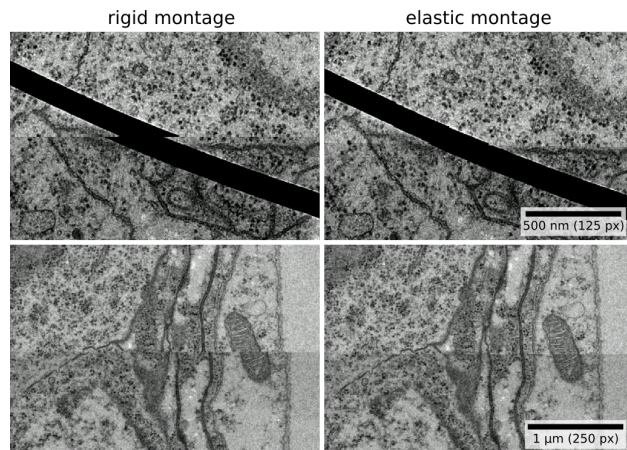
Shown are two areas along the diagonal cropped from an all to all matrix showing the number of matches that have passed the filters for each pair of sections from the *Drosophila* series. Numbers are encoded as gray values (see scale). Both panels show that the number of matches decreases with increasing distance of two sections in the series. The left panel shows the effect of two compromised sections (128 and 129) where more than 50% of the surface was covered with artifacts. Compromised sections will have a reduced number of matches with all sections behind and ahead in the series. Sections behind and ahead of the compromised sections generate the number of matches that corresponds to their relative distance (arrows). The right panel shows the effect of a gap of five sections between sections 348 and 349. The number of matches is consistently reduced for the section before the gap in forward direction and for the section after the gap in inverse direction (arrows).

Supplementary Figure 5 | Spring forces.



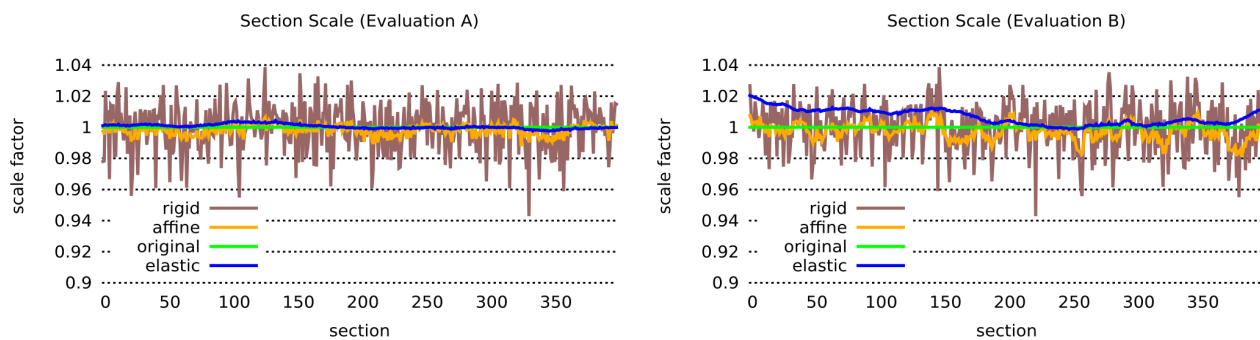
Each vertex p_0 is connected to other vertices p_i by an ideal spring. Each spring has a relaxed length l_i (shown for p_4). This relaxed length is zero for springs connecting to other images. The force of each spring can be calculated using Hooke's law summing up to the combined force vector F . The desired end-state of the system is where $F = 0$ for all vertices.

Supplementary Figure 6 | Elastic montaging compensates for non-rigid deformation.



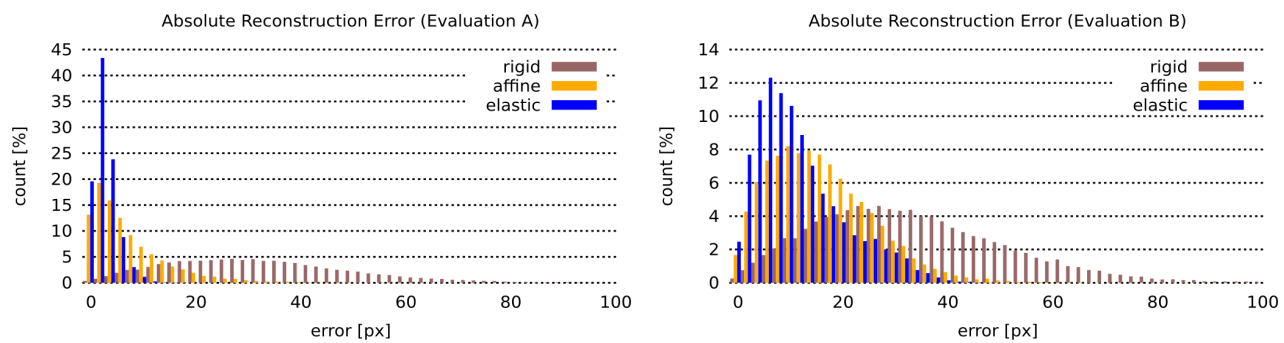
Lens distortion effects and heat-induced deformation of sections during imaging renders montaging with a rigid transformation per tile insufficient. Only an elastic approach can compensate for non-linear tile-to-tile distortion while minimizing the non-rigid deformation simultaneously. Note that the shown stitching errors do not result from non-optimal rigid alignment but exclusively from non-rigid deformation.

Supplementary Figure 7 | Comparison of average section scale factors after alignment of the evaluation series.



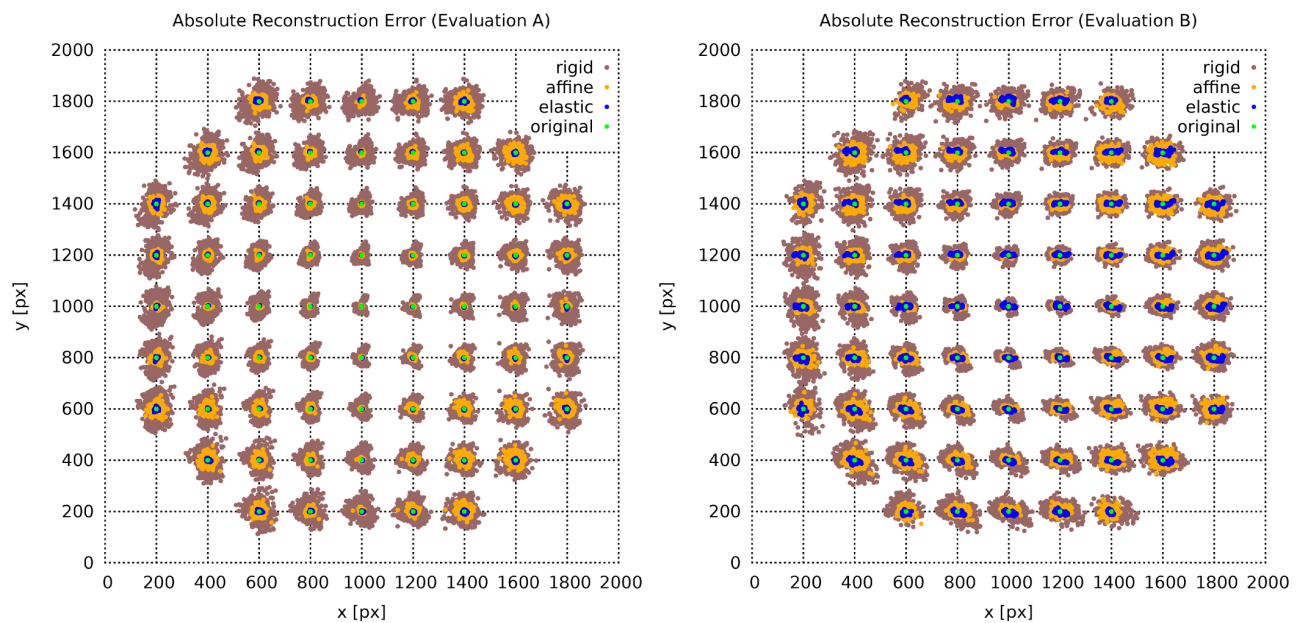
The average scale factor of a section relative to the non-deformed ground-truth is estimated through a least-squares approximation of the artificially introduced non-linear deformation by a similarity transformation (scale, rotation, translation). Since non-linear deformation has been introduced to all sections independently, no systematic scale change is expected across the series. All three methods preserve this property (**Supplementary Videos 2 and 3**). Elastic alignment almost perfectly recovers the original scale of all sections. As expected, the performance is better for series A where no signal change compromises the measured motion vectors.

Supplementary Figure 8 | Histograms of absolute point displacements after alignment of evaluation series A and B.



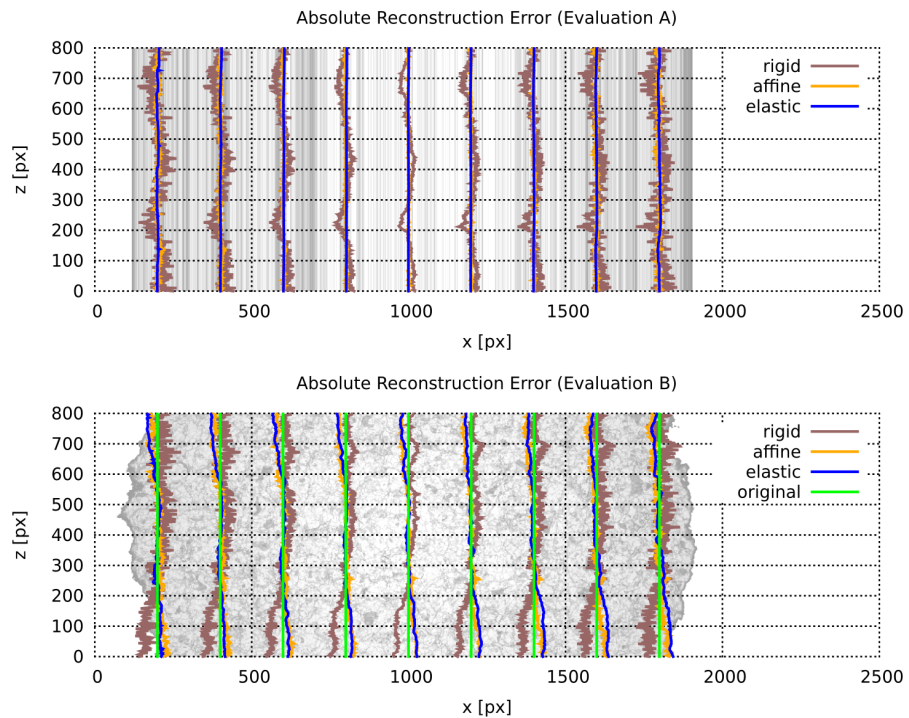
We have measured the absolute displacement in the x,y -plane relative to ground truth of each z-point of a sample of straight lines projected through the volume along the z-axis. Elastic alignment outperforms both methods. As expected, the result is slightly better in evaluation series A where no signal change compromises the measured motion vectors (left graph).

Supplementary Figure 9 | Projection of the x,y-location of each z-point of a sample of straight lines projected through the volume along the z-axis.



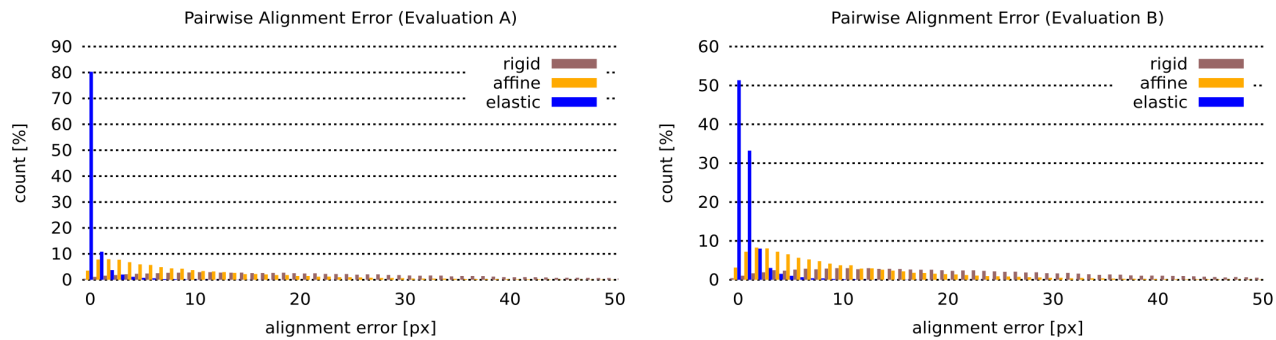
Elastic alignment very well recovers the original location of all points along the lines. As expected, the result is slightly better in evaluation series A where no signal change compromises the measured motion vectors (left graph). The displacement is minimal in the center of the volume and increases towards the periphery for all methods used. This effect is comparatively minimal in case of the elastic alignment.

Supplementary Figure 10 | Projection of the x,z-location of each z-point of a sample of straight lines projected through the volume along the z-axis.



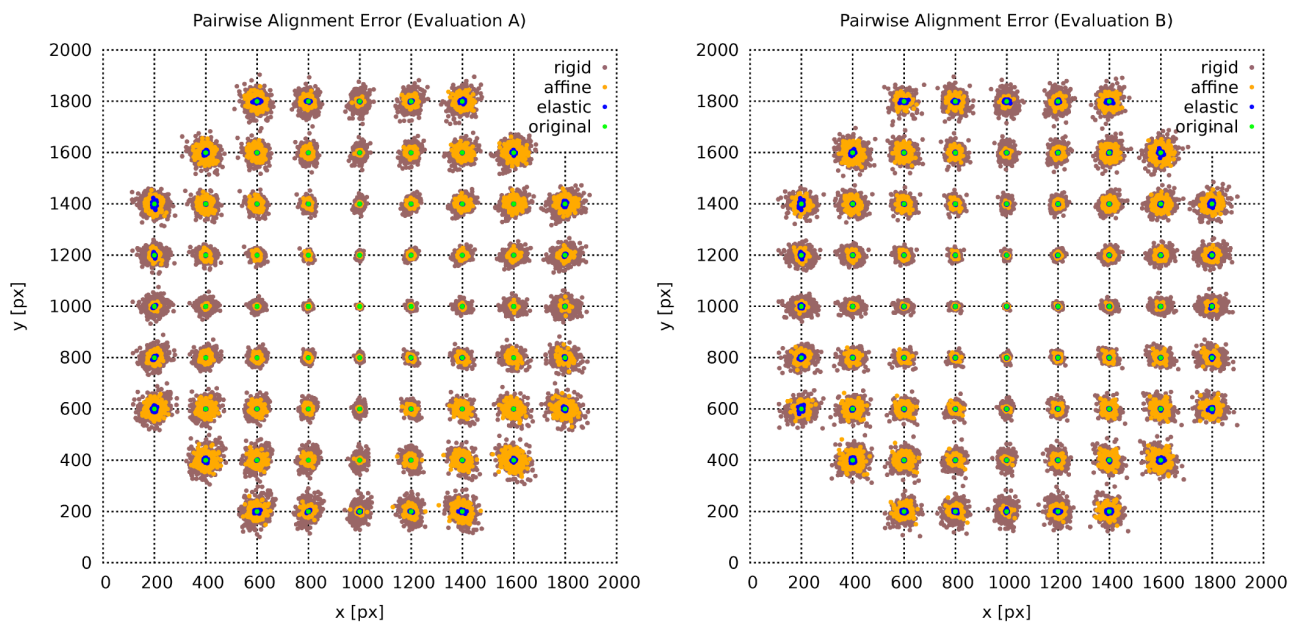
Elastic alignment very well recovers the original location of all points along the lines. As expected, the result is slightly better in evaluation series A where no signal change compromises the measured motion vectors (top graph). The displacement is minimal in the center of the volume and increases towards the periphery for all methods used. This effect is comparatively minimal in case of the elastic alignment. The background of the plot shows the corresponding x,z-section of the respective original evaluation series (note that in the top graph the texture of the volume does not change along the z-axis as all sections are the same).

Supplementary Figure 11 | Histograms of section-to-section pairwise point displacements after alignment of evaluation series A and B.



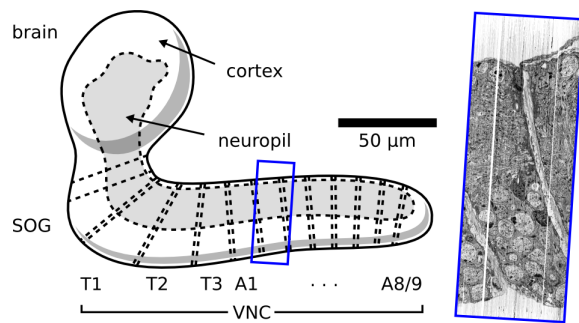
We have measured the pairwise displacement in the x,y -plane between adjacent sections for a sample of straight lines projected through the volume along the z -axis. Elastic alignment outperforms both linear methods significantly. As expected, the result is better in evaluation series A where no signal change compromises the measured motion vectors (left graph). Note that in evaluation series A for 80% of all sampled locations the pairwise displacement is below 1 pixel and for 90% below 2 pixel. In evaluation series B for 50% of all sampled locations the pairwise displacement is below 1 pixel and for 80% it is below 2 pixel.

Supplementary Figure 12 | Visualization of section-to-section pairwise point displacements after alignment of evaluation series A and B.



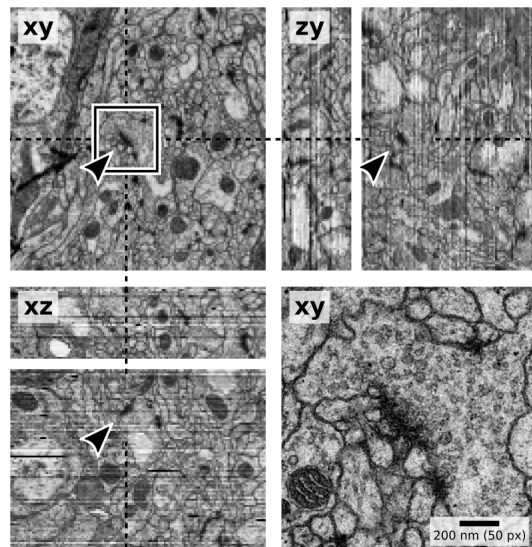
The pairwise displacement for each z-point of a sample of straight lines projected through the volume along the z-axis are displayed centered at the original x,y-location of the corresponding line. Elastic alignment outperforms both linear methods significantly. As expected, the result is better in evaluation series A where no signal change compromises the measured motion vectors (left graph). The pairwise displacement is minimal in the center of the volume and increases towards the periphery for all methods used. This effect is comparatively minimal in case of the elastic alignment.

Supplementary Figure 13 | Anatomical context of *Drosophila* larval ventral nerve cord ssTEM.



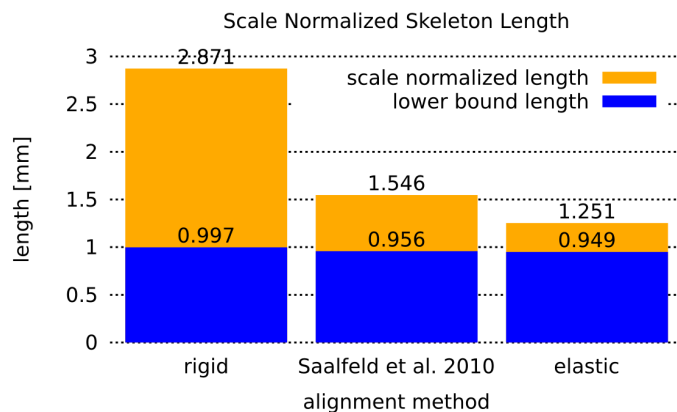
Cartoon based on a figure from Ito et al. 1995¹⁹. The blue box marks the approximate area from which the series of sections originates (note that the exact location of the series within abdominal segments is not known). The inset shows the sagittal plane at the midline through the elastically aligned volume. VNC - ventral nerve cord, SOG - subesophageal ganglion, T1–3 - thoracic segments, A1–9 - abdominal segments.

Supplementary Figure 14 | Synapses are detectable in both lateral and axial views after elastic reconstruction.



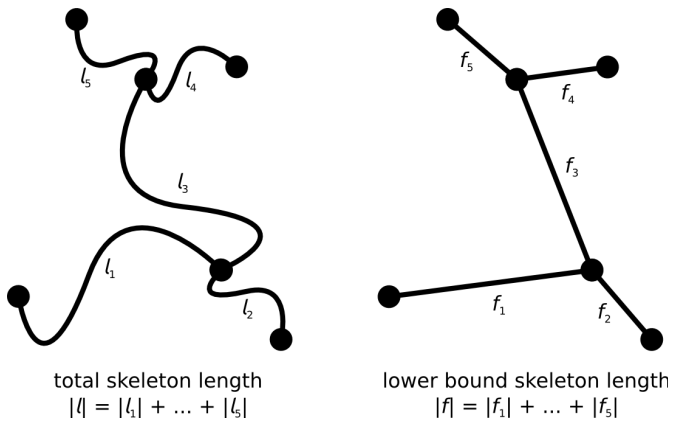
A synapse (arrowheads) is shown in lateral (**xy**) and two axial (**zy**, **xz**) views of the elastically aligned *Drosophila* dataset. The top left lateral and both axial views were generated from the section series scaled down to isotropic resolution. The area highlighted by a black square is shown at the original lateral resolution of 4nm/px (**xy**, bottom right). While single vesicles can be distinguished only in the high resolution image of the section, it is possible to identify synapses by their increased pre-synaptic density at axial resolution. The white bands visible in the axial panels are missing sections. The dashed lines indicate the locations of the respective axial sections.

Supplementary Figure 15 | Comparison of three alignment methods applied to the *Drosophila* series using the total length of manual skeleton annotation.



The first method is a sequential alignment using a rigid transformation per section estimated from automatically extracted features (rigid). The second method estimates a rigid transformation per each mosaic tile globally minimizing the total square displacement of automatically extracted feature correspondences (Saalfeld et al. 2010)⁸. The third is our new elastic method initialized with the result of the second method. We report the total length of manually traced neuronal arbor skeletons with all edge lengths normalized by a local scale factor s (**Equation 3**). The local scale factor s for each skeleton edge (p,q) is the average scale factor of the contributing sections at p and q relative to the original image size. We compare the total skeleton length with an approximate lower bound skeleton length calculated from all edges between branch and end nodes of the skeleton replaced by straight lines (**Supplementary Fig. 16**).

Supplementary Figure 16 | Total skeleton length and lower bound skeleton length.



We compare the total skeleton length l with a lower bound skeleton length f that serves as an approximation of the minimal possible skeleton length and is robust with respect to alignment errors. The lower bound length f is the sum of the length of all edges between branch and end points of the skeleton replaced by straight lines.

Supplementary Tables

Supplementary Table 1 | Overview of reconstructed ssTEM datasets.

	<i>C. elegans</i> three-fold stage embryo	<i>D. melanogaster</i> first instar larva ventral nerve cord
TEM recording mode	scanned from film	digital imaging of overlapping tiles
Number of sections	803	458
Image tiles per section	1	>70
Tile size	6,160×4,640	2,048×2,048 pixels
Bits per pixel	8	16
Section canvas size	6,160×4,640	~22,000×17,000 pixels
Lateral resolution	4 nm/pixel	4 nm/pixel
Section thickness	50 nm	45 nm
Missing sections	25*	2 + 5
Total number of images	803	33,051 (with content) 77,017 total**
Size in GB	21	258 (with content) 602 total*
Processing time	~ 12 hours	~ one week

*The record of the series declares missing sections at 9 different places, ranging from 1 up to 7 sections missing. Without knowing that in prior, we were able to identify the four larger gaps and their approximate sizes by analyzing the ratio of block matches that passed local and global filters (**Supplementary Fig. 4**). **Many tiles imaged on the periphery of the specimen contain only background. Our previously published feature based method8 explicitly removes these from the alignment because no corresponding image context can be found between images within and/or across sections.

Supplementary Note

Triangle sizes

A triangle of springs has two families of cost minima in the plane: (1) at rigid transformations and (2) at rigid transformations flipped. That is, for all local deformations smaller than the size of a triangle, the mesh will drag towards a rigid transformation. For larger deformation, it may fold. The resolution of the triangle meshes should thus be chosen such that the expected local deformation does not exceed the side-length of a triangle.

The mesh resolution chosen for our experiments (24 in the *C. elegans* series and 48 in the *Drosophila* series) is a trade-off between alignment accuracy and execution speed. Since correspondences are searched for each vertex of the mesh by block matching, increasing the resolution of the mesh improves accuracy but increases runtime. Around discontinuities like section folds or tears, a region of up to the side-length of a triangle suffers from potentially inaccurate alignment. The error decreases with increasing distance to the discontinuity and reaches ‘normal’ values at the boundary to an adjacent triangle if for all its vertices a block match could be identified. Although our method in its present form does not explicitly model discontinuous deformation, it performs robustly in their presence. A discontinuous deformation in one section of a series will not compromise the alignment of the series because it will be overruled by all sections in their local neighborhood.

Regularized global affine alignment

In situations where only pairwise alignment is required (e.g. as initialization for block matching), higher order, less constrained transformation models can be used (e.g. an affine transformation). For groupwise alignment (series alignment or montaging), propagation of arbitrary scaling or shearing must be prevented. Using an unconstrained affine transformation in a global approach⁸ has its optimum at a scale factor of zero. Using it sequentially would lead to increasing scale change and random shear (data not shown). We have therefore used a rigid transformation as a regularization term for the affine transformation which effectively prevents a global solution from introducing systematic shear and scale. Let \mathbf{A} be an affine transformation and \mathbf{R} be a rigid transformation. Both transformations are estimated by means of least-squares correspondence point displacement. The desired regularized affine transformation according to a regularization factor λ ranging between zero and one is then the linearly interpolated transformation $\mathbf{B}=(1-\lambda)\mathbf{A}+\lambda\mathbf{R}$. In our experiments, we have used a regularization factor $\lambda=0.1$ which proved a good tradeoff between regularization and the affine transformation’s ability to cope with non-rigid deformation.

Simultaneous alignment and recognition

Similar to the original application for robust object recognition⁷, we use local image feature matches not only to align overlapping images but as well to identify overlapping images in non-initialized montages and to automatically estimate the range of sections in a series to be connected during elastic alignment (**Fig. 1a**). To that end, we match the features for each pair of images. Where no correspondences for two images could be identified, the conclusion can be drawn that they do not contain similar enough image content. When exploring non-initialized montages, all image pairs need to be analyzed. For identifying the range of sections to be compared in a series, we analyze pairs of increasing distance until matching has failed repeatedly. That way, the complexity of the comparison is greatly reduced while still offering the opportunity to bridge across artificially distorted sections in the series. We have used this recognition capability to exclude empty and disconnected tiles from the *Drosophila* dataset. Out of 77,017 images, 33,499 images were automatically recognized as non-empty connected content and aligned, all other tiles were excluded from the dataset. We have later manually removed 448 tiles that were not showing parts of the specimen but were connected to section montages through texture from artifacts and background, resulting in 33,051 images all contributing to the reconstruction of the specimen.

Imaged datasets

We have applied our elastic alignment method to two outstanding ssTEM datasets (**Supplementary Table 1**) and one series of sections imaged by light microscopy. The *C. elegans* dataset showing a three-fold stage embryo was generated in 2003 by Richard Fetter in the laboratory of Cori Bargmann. The timed embryo collection was prepared by high pressure freezing and freeze-substitution. Sections were cut and imaged on a JEOL 1200EX TEM using Kodak 4489 film. The negatives were then digitized with an Epson flat bed scanner. Each negative was 3.25"×4" in physical size.

The *D. melanogaster* dataset showing 1.5 segments of the ventral nerve cord of a first instar larva was acquired by Richard Fetter and Albert Cardona at the Janelia Farm Research Campus using an FEI Tecnai T20 transmission EM electron microscope. Each section was imaged with a Gatan 895 4,096×4,096 pixels digital camera as a series of overlapping image tiles. Typically about 150 tiles were recorded per section. More than half of the acquired tiles, mostly on the periphery of the ventral nerve cord, lacked any image content and were automatically removed during the alignment procedure. During serial sectioning, inevitably, some sections are lost. For the *C.elegans* series this happened in nine different places and for *Drosophila* it happened twice.

The light microscopy dataset has been generated using Array Tomography¹⁵ by Forrest Collman, Nick Weiler, Kristina Micheva and Stephen Smith. In this method the tissue is sectioned into a series of ultra-thin sections achieving an axial resolution far beyond that of optical sectioning techniques. Each section is repeatedly stained with antibodies, imaged by light microscopy and destained. In this way it is possible to study co-localization of potentially many proteins in the same tissue. Our elastic method can be used to obtain the 3d reconstruction of the section series after each staining cycle. In the particular case shown in **Supplementary Videos 12–14** we reconstructed a sample series of 43 serial sections of 70 nm thickness each from barrel cortex of an adult Line H YFP mouse²⁰ expressing YFP in a subset of layer 5b pyramidal cells, pial surface at the top. Each section shows three fluorescent channels imaged by light microscopy as an arbitrary RGB overlay, DAPI (blue), YFP (green) and Synapsin (red). Interestingly, the 3d rendering (**Supplementary Video 14**)²¹ reveals that given the ultra-thin sections and the limits of resolution imposed on light-microscopy, in this dataset, the axial resolution (70 nm) is better than the lateral one.

Implementation and Availability

We have implemented our method in the Java programming language. We have included it into our Open Source library (<http://pacific.mpi-cbg.de/cgi-bin/gitweb.cgi?p=mpicbg.git>) that we distribute with Fiji¹⁴. We provide two standalone plugins for Fiji. The plugin Elastic Stack Alignment takes a stack of images and aligns it as a section series. The stack can be virtualized such that only the necessary images for every step are loaded, allowing an off-the-shelf desktop computer to align very large series. The plugin Elastic Montage implements the automatic elastic registration of 2d image tiles, and is used for montaging mosaics from series of overlapping image tiles where the tiles have non-linear relative deformations. Tiles are provided as an unordered stack of images. The plugin estimates the configuration of the mosaic automatically. In addition, we integrated both elastic montaging and elastic series alignment into the TrakEM2 Open Source software included in Fiji¹². TrakEM2 virtualizes access to all image tiles and provides an interactive point-and-click environment to montage or register subsets of the data and to manually alter the results of the automatic elastic registration. In TrakEM2 our elastic registration method complements many other tools to organize, align, adjust, segment, visualize and analyze large and small electron microscopy datasets (Cardona et al. manuscript in preparation). Each image can be transformed by a sequence of arbitrary transformations without degrading its quality by consecutive rendering steps. That is, elastic montaging and series alignment can be executed on image data that was previously corrected for lens-distortion²² or pre-aligned using a different method⁸. Likewise, the elastically aligned series, individual images, or sections may be deformed subsequently to correct for alignment errors or systematic distortion. This is of particular interest since the proposed image-based alignment method can compensate for independent section-

deformation only and will preserve systematic distortion such as e.g. compression of the volume along the cutting direction.

All expensive independent operations are parallelized for optimal use of a single computer with multiple CPU cores accessing shared random access memory (RAM). Further scalability may be achieved by distributing the dominant operation: independent image-to-image pairwise block-matching and filtering to a cluster of independent computers with non-shared memory. To establish the required infrastructure for this is subject of future improvements of the implementation.

References

20. Feng et al. *Neuron* **28**(1), 41–51 (2000).
21. Schmid, B., Schindelin J., Cardona A., Longair M. and Heisenberg M. *BMC Bioinformatics* **11**: 274 (2010).
22. Kaynig, V., Fischer B., Müller E., and Buhmann J.M. *J Struct Biol* **171**(2):163–173 (2010).